Pressure-induced phase transition and phonon softening in h-Lu$_{0.6}$Sc$_{0.4}$FeO$_3$

K. A. Smith,[1] S. P. Ramkumar [ORCID],[2] N. C. Harms,[1] A. J. Clune,[1] S.-W. Cheong,[3,4,5] Z. Liu,[6]
E. A. Nowadnick,[2] and J. L. Musfeldt [ORCID][1,7,*]

[1]*Department of Chemistry, University of Tennessee, Knoxville, Tennessee 37996, USA*
[2]*Department of Materials Science and Engineering, University of California, Merced, California 95343, USA*
[3]*Department of Physics and Astronomy, Rutgers University, Piscataway, New Jersey 08854, USA*
[4]*Rutgers Center for Emergent Materials, Rutgers University, Piscataway, New Jersey 08854, USA*
[5]*Laboratory for Pohang Emergent Materials, Pohang Accelerator Laboratory and Max Planck POSTECH Center
for Complex Phase Materials, Pohang University of Science and Technology, Pohang 790-784, Korea*
[6]*Department of Physics, University of Illinois Chicago, Chicago, Illinois 60607-7059, USA*
[7]*Department of Physics and Astronomy, University of Tennessee, Knoxville, Tennessee 37996, USA*

We combine diamond anvil cell techniques, synchrotron-based infrared and Raman scattering spectroscopies, a symmetry analysis, and complementary lattice dynamics calculations to explore the pressure-driven phase transition in multiferroic h-Lu$_{0.6}$Sc$_{0.4}$FeO$_3$. Comparison of the measured and predicted phonon patterns reveals a $P6_3cm \rightarrow P\bar{3}c1$ structural transition at 15 GPa. Symmetry breaking across the polar $\rightarrow$ antipolar transition takes place via changes in the bipyramidal tilting direction and Lu/Sc displacement pattern, analogous to the strain-driven K_3 distortion pathway in h-LuFeO$_3$ and temperature-induced transitions in the rare-earth manganites.

I. INTRODUCTION

Rare-earth ferrites such as LuFeO$_3$ are linear magnetoelectrics [1]. As an iron oxide, this material attracted early attention from the earth sciences community, where it was shown that T_N increases linearly under pressure due to systematic changes in the Fe-O-Fe superexchange, and that the optical band gap decreases between 40 and 50 GPa due to the diminishing importance of the magnetic phase (due to a high $\rightarrow$ low spin crossover) [2]. This mechanism was recently confirmed by x-ray emission spectroscopy [3]. LuFeO$_3$ is closely related to LuFe$_2$O$_4$, a system in which charge ordering, a structural distortion, and magnetic ordering combine to reveal an exotic magnetic field-temperature phase diagram [4–10]. It also plays a central role in the family of multiferroic (LuFeO$_3$)$_m$/(LuFe$_2$O$_4$)$_n$ superlattices [11–15] where interface strain drives near-room-temperature performance. Clearly, LuFeO$_3$ is an important platform for the development of a number of important Fe-based multiferroics. Unfortunately, hexagonal LuFeO$_3$ can only be grown in thin-film form, which limits the types of experiments that can be performed and hence our understanding of the material. On the other hand, A-site substitution is a well-known strategy for stabilizing metastable phases and tuning the properties of perovskites [16,17]. Here, Sc substitution on the Lu site creates hexagonal single crystals with the chemical formula h-Lu$_{0.6}$Sc$_{0.4}$FeO$_3$ [18,19]. This enables us to elucidate the structural phase diagram using pressure, which was not possible before. This multiferroic material hosts robust polarization ($\approx 1\ \mu$C/cm^2), which can be switched at room

temperature. T_C is well above 1000 °C, and T_N is on the order of 170 K [18]. Given the crucial role of pressure, strain, and interface effects in stabilizing and tuning the family of hexagonal iron oxide materials, we resolved to examine the structural phases and symmetry progression of one of the simplest members of this series—the linear magnetoelectric h-Lu$_{0.6}$Sc$_{0.4}$FeO$_3$.

Lu$_{0.6}$Sc$_{0.4}$FeO$_3$ is isostructural to h-YMnO$_3$, with a crystal structure that consists of layers of corner-connected iron-oxide trigonal bipyramids separated by a layer of Lu/Sc cations. At ambient pressure, it crystallizes in the polar $P6_3cm$ space group. As shown in Fig. 1, $P6_3cm$ is established by the condensation of a structural distortion that transforms like the K_3 irreducible representation of the high-symmetry space group $P6_3/mmc$. The K_3 distortion consists of a tilting of the iron-oxide bipyramids and a displacement of the Lu/Sc atoms along the c axis. This distortion is described by a two-dimensional order parameter (Q, Φ), where Q gives the amplitude of the distortion, and the phase Φ describes the direction in which the iron-oxide bipyramids tilt. h-Lu$_{0.6}$Sc$_{0.4}$FeO$_3$ is an improper ferroelectric, so the polarization is induced via a nonlinear coupling to the K_3 distortion. Three distinct structural phases can be established by varying the phase Φ of the K_3 distortion. As shown in Fig. 1, $\Phi = 0$ establishes the polar $P6_3cm$ structure, and the bipyramids tilt directly towards their shared planar oxygen. Rotating the tilting direction to $\Phi = \pi/6$ establishes the antipolar structure $P\bar{3}c1$ (right-hand side of Fig. 1), where now the Lu/Sc atoms display a down-0-up displacement pattern. Any other value of Φ establishes a structure with space group $P3c1$.

There are several strategies for tuning the structure and properties of h-LuFeO$_3$ and related systems. Previous work
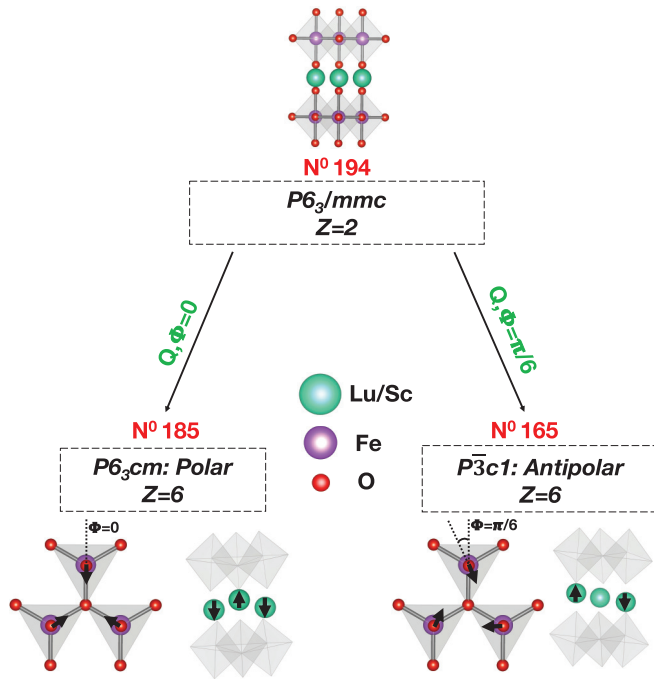
*musfeldt@utk.edu

FIG. 1. Group-subgroup relationship along with the corresponding distortion modes between high-symmetry $P6_3/mmc$ and low-symmetry $P6_3cm$ (polar)/$P\bar{3}c1$ (antipolar) structures of hexagonal (Lu/Sc)FeO$_3$. The K_3 mode distortions are given in terms of a two-component order parameter (Q, Φ) similar to the hexagonal manganites [20].

reveals that epitaxial strain [6,21,22] in LuFeO$_3$ thin films modulates the K_3 structural distortion. Compressive strain increases the K_3 amplitude [23,24], which raises T_N and is predicted to enhance the polarization [23,24]. Hydrostatic pressure is another well-known stimulus for controlling crystal structure, although the response of LuFeO$_3$ and its relation to strain-driven effects in this system remains underexplored. Comparison with other hexagonal oxides suggests multiple candidate distortion pathways [20,25–27]. For example, both RMnO$_3$ [28–31] and RInO$_3$ [32] display a pressure-induced transition from hexagonal to orthorhombic (*Pbnm*) structure, with the critical pressure depending on the rare-earth cation (R). As another example, chemical substitution on the indium site in h-RInO$_3$ applies an effective in-plane strain and tunes the ground state from $P6_3cm$ to $P\bar{3}c1$ [27].

To explore how ferroelectricity evolves under pressure, and to distinguish between likely distortion pathways, we combined synchrotron-based infrared absorption and Raman scattering spectroscopies with a symmetry analysis and lattice dynamics calculations to reveal the vibrational properties of h-Lu$_{0.6}$Sc$_{0.4}$FeO$_3$. Using these sensitive, site-specific techniques [10,33–36], we find a critical pressure (P_C) of 15 GPa above which an infrared-active E_1 symmetry phonon near 500 cm^{-1} disappears and several low-frequency Raman-active modes soften. Based upon a comparison of predicted versus experimental vibrational patterns for different candidate space groups, we assign the high-pressure phase in h-Lu$_{0.6}$Sc$_{0.4}$FeO$_3$ as $P\bar{3}c1$ (Fig. 1). The pressure-driven polar

$\leftrightarrow$ antipolar transition is thus $P6_3cm \leftrightarrow P\bar{3}c1$. We discuss the relevant order parameters and phase progression under pressure and compare the result with the mechanism under compressive strain. Lastly, we examine the structure-property relationships that can be unraveled by analogy with the hexagonal rare-earth manganese and indium oxides. These ideas lead to several interesting design and control schemes for ferrite-based materials.

II. METHODS

A. Experimental methods

High-quality h-Lu$_{0.6}$Sc$_{0.4}$FeO$_3$ single crystals were grown using optical floating zone techniques as described previously [18]. Samples were loaded into a symmetric diamond anvil cell along with a pressure medium and an annealed ruby ball. Care was taken to optimize optical density in order to reveal the excitations of interest. KBr or a hydrocarbon-based vacuum grease (petroleum jelly) was used as the pressure medium to assure a quasihydrostatic environment for Raman scattering and far-infrared experiments, respectively. Diamonds with 300 or 400 μm culet sizes and stainless steel gaskets with 100 μm holes were employed. Ruby fluorescence was used to monitor pressure [37]. We point out that any high-pressure experiment involving a diamond anvil cell is hydrostatic under optimal conditions only to about 6 or 8 GPa. This assumes that there are no problems with the gasket and that a suitable pressure-transmitting medium is employed. Above 6 or 8 GPa, there are always nonhydrostatic effects. By monitoring the shape of the ruby fluorescence as well as peak shapes in the sample spectrum (and assuring that linewidths do not become too wide), we can confirm that there are no major changes across the pressure range of interest here and that Lu$_{0.6}$Sc$_{0.4}$FeO$_3$ remains quasihydrostatic.

Synchrotron-based infrared spectroscopy (50–650 cm^{-1}; 4 cm^{-1} resolution; transmittance geometry) and Raman scattering (70–3600 cm^{-1}, $\lambda_{\text{excit}} = 532$ nm; $\approx$1 mW power; 1200 gr/mm grating, 90 s integration, averaged two times) were carried out under pressure using the 22-IR-1 beamline at the National Synchrotron Light Source II at Brookhaven National Laboratory. All data were collected at room temperature. For comparison, we also performed infrared absorption and Raman scattering measurements at ambient conditions (i.e., without a diamond anvil cell). Vibrational mode assignments were made by comparison with literature data [38] and our lattice dynamics calculations for various candidate space groups as discussed in the main text.

B. Theoretical methods

We perform density functional theory (DFT)+U [39,40] calculations using the projector augmented wave (PAW) [41] method as implemented in VASP [42]. We employ the Liechtenstein *et al.* [43] formulation of DFT+U, with on-site Coulomb and exchange interactions of $U = 4.5$ eV and $J = 0.95$ eV, respectively, on iron, in agreement with previous calculations [44]. We use the PBEsol functional [45], a 600 eV energy cutoff on the plane-wave basis, and convergence criteria of 10^{-8} eV on the total energy and 2 meV/Å on the forces. We employ a $4 \times 4 \times 2$ Γ-centered k-point mesh
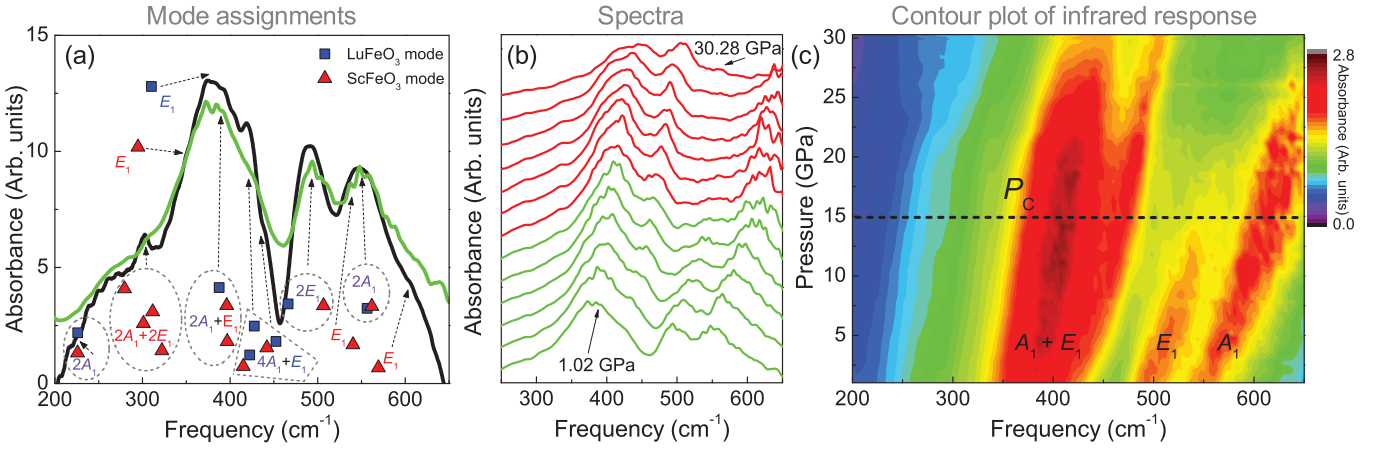
FIG. 2. (a) Traditional (black) and diamond anvil cell (green) infrared spectrum of $Lu_{0.6}Sc_{0.4}FeO_3$ at ambient conditions. Theoretical mode positions and intensities of the end member compounds $LuFeO_3$ and $ScFeO_3$ in the $P6_3cm$ space group are shown with blue squares and red triangles, respectively. The modes are grouped together to show how we assign various predicted excitations to the observed experimental features. Table I summarizes these assignments in tabular rather than graphical form. The theoretically predicted mode frequencies and symmetries for $LuFeO_3$ and $ScFeO_3$ in the $P6_3cm$ space group are also provided in Tables S5 and S6 of the Supplemental Material [46]. (b) Infrared response of $Lu_{0.6}Sc_{0.4}FeO_3$ as a function of pressure. The spectra are offset for clarity, and the color (green vs red) indicates the phase. (c) Contour plot of the same data as in panel (b). The critical pressure (P_C) is indicated with a dashed line at 15 GPa.

to sample the Brillouin zone of the 30-atom unit cell of the $P6_3cm$ and $P\bar{3}c1$ structures, a $4 \times 4 \times 4$ Γ-centered mesh for the 20-atom cell of the orthorhombic $Pbnm$ structure, and an $8 \times 8 \times 2$ Γ-centered mesh to sample the 10-atom cell of $P6_3/mmc$.

All calculations are performed for single A-site compounds, that is, we perform calculations for $LuFeO_3$ and $ScFeO_3$, but we do not consider compositions with mixed Lu/Sc. All calculations presented in the main text are done with A-type antiferromagnetic (A-AFM) order imposed. We explore other magnetic configurations in the Supplemental Material [46].

We use density functional perturbation theory (DFPT) [47–49] as implemented in VASP to compute the Γ-point phonon frequencies, Born effective charge tensors ($Z^*_{\kappa,\alpha\beta}$ for atom κ and displacement directions $\alpha, \beta = 1, 2, 3$), and

eigendisplacements ($X_{\kappa,\beta}$). We then calculate the infrared intensity of phonon mode m using PHONOPY [50,51] and the PHONOPY-SPECTROSCOPY package [52,53]:

$$I_{IR}(m) = \sum_\alpha \left| \sum_\kappa \sum_\beta Z^*_{\kappa,\alpha\beta} X_{\kappa,\beta}(m) \right|^2. \quad (1)$$

We also use PHONOPY-SPECTROSCOPY [52,53] to calculate the scalar Raman intensity (I_{Raman}). This is constructed from the Raman susceptibility tensor $\alpha^m_{\alpha\beta}$, which is proportional to the change in the electric polarizability $\chi_{\alpha\beta}$ with respect to displacement amplitude $Q(m)$ along mode eigenvector m, and it can be related to the macroscopic high-frequency dielectric constant (ϵ^∞) [52],

$$\alpha^m_{\alpha\beta} \propto \frac{\partial \chi_{\alpha\beta}}{\partial Q(m)} \equiv \frac{\partial \epsilon^\infty_{\alpha\beta}}{\partial Q(m)} \approx \frac{\Delta \epsilon^\infty_{\alpha\beta}}{\Delta Q(m)}. \quad (2)$$

TABLE I. Summary of mode assignments for h-$Lu_{0.6}Sc_{0.4}FeO_3$ at ambient conditions in the $P6_3cm$ space group. For assignments containing both Lu and Sc, we list the frequency of the Lu mode first.

Experimental peak frequency (cm^{-1})	Lu/Sc mode	Assigned theoretical mode frequencies (cm^{-1})	
		A_1	E_1
225	Both	226.1, 225.8	
302	Sc	301.1, 311.6	294.9, 322.1
350	Sc		294.9
375	Lu		310.3
385	Both	387.5, 396.2	396.8
420	Both	427.7, 422.4	415.1
440	Both	452.4, 442.0	
490	Both		466.4, 506.7
540	Sc		540.3
550	Both	556.5, 561.8	
602	Sc		569.4

Using the central-difference method to calculate the derivatives, the Raman susceptibility can then be expressed as

$$\alpha_{\alpha\beta}^m = \frac{\Omega}{4\pi}\left[-\frac{1}{2}\frac{\epsilon_{\alpha\beta}^\infty(-m)}{\Delta Q(m)} + \frac{1}{2}\frac{\epsilon_{\alpha\beta}^\infty(m)}{\Delta Q(m)}\right], \qquad (3)$$

where Ω is the unit cell volume and $\epsilon_{\alpha\beta}^\infty(\pm m)$ is the dielectric tensor computed when the atoms are displaced by $\pm\Delta Q$ along mode eigenvector m. The scalar Raman intensity (I_{Raman}) to be compared to the experimental measurements is then obtained by averaging the Raman susceptibility tensor $\alpha_{\alpha\beta}^m$ over the measurement geometry, which for a setup with the incident beam direction, its polarization, and the observation direction all perpendicular to each other yields [53,54]

$$I_{\text{Raman}} = \frac{45}{9}(\alpha_{11} + \alpha_{22} + \alpha_{33})^2 + \frac{7}{2}\big[(\alpha_{11} - \alpha_{22})^2$$
$$+ (\alpha_{22} - \alpha_{33})^2 + (\alpha_{11} - \alpha_{33})^2$$
$$+ 6(\alpha_{12}^2 + \alpha_{23}^2 + \alpha_{13}^2)\big]. \qquad (4)$$

III. RESULTS AND DISCUSSION

A. Infrared response of $Lu_{0.6}Sc_{0.4}FeO_3$ under pressure

Figure 2 summarizes the vibrational response of $Lu_{0.6}Sc_{0.4}FeO_3$ under pressure. We begin by comparing the infrared absorption measured in the diamond anvil cell with that taken using traditional techniques. They are in good overall agreement. We assign the vibrational modes using our lattice dynamics calculations of the two end members $LuFeO_3$ and $ScFeO_3$. The frequencies, overall pattern, and relative intensities of the predicted modes are an excellent match with the measured spectrum [Fig. 2(a)]. Note that a number of features are grouped, which is expected for a system like $Lu_{0.6}Sc_{0.4}FeO_3$ which has a complex mode pattern and certain aspects of a solid solution with both Lu and Sc substitution on the *A* site. A complete list of mode assignments is provided in Table I. From Fig. 2(a) it is clear that the computed $LuFeO_3$ and $ScFeO_3$ modes are clustered together for the two materials (both in terms of frequency and intensity). There are only a few outliers, such as those around 300 and 570 cm^{-1} in $ScFeO_3$ with no corresponding modes for $LuFeO_3$. Therefore, for the subsequent analysis in the rest of this work, we consider only the $LuFeO_3$ phonon frequencies/intensities for comparison with the experimental spectra.

Figure 2(b) shows how the infrared spectrum of $Lu_{0.6}Sc_{0.4}FeO_3$ evolves with increasing pressure. There are two striking trends: the divergence of A_1 and E_1 modes that are part of the broad feature centered near 380 cm^{-1}, and the progressive disappearance of the E_1 mode near 500 cm^{-1}. Based upon these trends, we identify a critical pressure P_C at 15 GPa. Figure 2(c) displays the same progression in the form of a contour plot. The intensity changes at P_C are clearly evident.

Group theory predicts several possible structural transition pathways that can occur under pressure. One possibility is that the system transitions from $P6_3cm$ to the high-symmetry $P6_3/mmc$ structure. Figure S1 summarizes three possi-

ble routes for this transformation: (i) $P6_3cm \rightarrow P6_3mc \rightarrow P6_3/mmc$; (ii) $P6_3cm \rightarrow P6_3/mcm \rightarrow P6_3/mmc$; and (iii) $P6_3cm \rightarrow P6_3/mmc$ [46]. The first two are two-step pathways, whereas the third is a single-step pathway. Examining the experimental data, we observe only one distinct transition as a function of pressure ($P_C = 15$ GPa). This suggests that the structural phase transition in $Lu_{0.6}Sc_{0.4}FeO_3$ occurs in a single step, ruling out the possibility of two-step processes such as those shown in Fig. S1 [46]. In addition, the high-symmetry $P6_3/mmc$ structure is stable with respect to Γ_2^- and K_1 phonons that establish the intermediate structures $P6_3mc$ and $P6_3/mcm$, respectively (Tables S2 and S3 in the Supplemental Material [46]). This leaves the possibility of a direct transition to the $P6_3/mmc$ space group. Other options include the K_3 order parameter rotating under pressure to establish a structure with symmetry $P\bar{3}c1$ (Fig. 1), or the system staying in $P6_3cm$ with no symmetry change under pressure. A final possibility is a transition to the orthorhombic $Pbnm$ structure under pressure. As noted above, a pressure-induced hexagonal-orthorhombic transition has been reported in the manganites [28–31] and indites [32].

To determine the space group of the high-pressure phase of $Lu_{0.6}Sc_{0.4}FeO_3$, we compare the predicted mode frequencies and intensities of $P6_3/mmc$, $P6_3cm$, $P\bar{3}c1$, and $Pbnm$ to the measured infrared spectrum at 20 GPa. Figure 3 summarizes the results of this comparison. It is immediately apparent that the $P6_3/mmc$ fit is too sparse and largely inferior, guiding our assignment of the high-pressure phase toward the other candidates. $Pbnm$ has two high-intensity modes near 250 cm^{-1} that are unassigned. This is problematic, especially since there are no high-intensity spectral features in the vicinity. This leaves polar $P6_3cm$ and antipolar $P\bar{3}c1$ as the remaining candidates [Figs. 3(b) and 3(c)]. A comparison of the predicted and measured mode patterns below 300 cm^{-1} provides a key test. Examination reveals that $P6_3cm$ offers no assignment for the 200 cm^{-1} peak in the measured spectrum, and while it provides two high-intensity modes near 275 and 320 cm^{-1}, they are not nearly so strong in the experimental response. In contrast, $P\bar{3}c1$ offers three low-frequency features with modest intensities that are in reasonable agreement with the measured response. We therefore find the $P\bar{3}c1$ space group to be the best match [Fig. 3(c)], and we assign it as the symmetry of the high-pressure phase.

B. Raman scattering response under pressure

To complement our infrared work, we performed Raman scattering measurements on $Lu_{0.6}Sc_{0.4}FeO_3$ under pressure up to 30 GPa (Fig. 4). Unlike the infrared response, the Raman spectrum has only a few distinct well-isolated peaks and peak clusters. This makes mode assignment straightforward. The majority of the Raman-active modes harden with pressure, a typical trend. These features also display linewidth narrowing and very slight slope changes in the vicinity of $P_C = 15$ GPa [Figs. 4(c)–4(e)]. There is no evidence for a symmetry modification within our sensitivity. There is, however, a low-frequency cluster containing peaks at 88 and 111 cm^{-1} that softens with increasing pressure [Fig. 4(a)]. Remarkably, the onset of this mode softening coincides with the 15 GPa critical pressure observed in the infrared. These findings provide
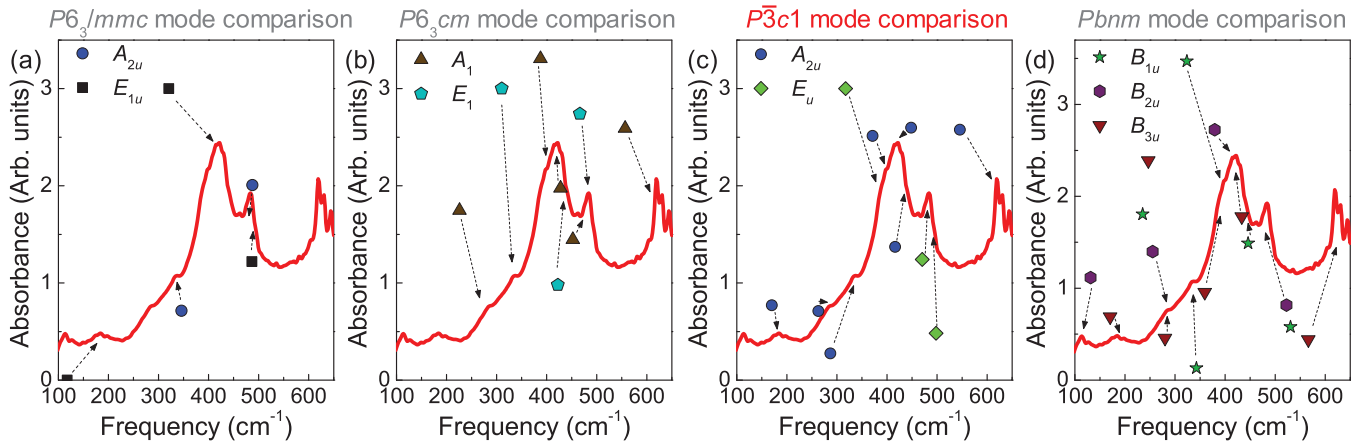
FIG. 3. Infrared spectrum of $Lu_{0.6}Sc_{0.4}FeO_3$ in the high-pressure phase (at 20 GPa) compared with calculated mode positions, symmetries, and intensities for four candidate high-pressure space groups: (a) $P6_3/mmc$, (b) $P6_3cm$, (c) $P\bar{3}c1$, and (d) $Pbnm$. The calculations are performed for the end-member compound $LuFeO_3$. The match between experiment and theory for the space group $P\bar{3}c1$ is superior and indicated in red. The calculated mode frequencies and symmetries for all space groups considered are summarized in the Supplemental Material [46].

additional evidence for a structural phase transition at this pressure.

By combining theoretically predicted mode frequencies and intensities with our experimental data, we assign and track various features as a function of pressure. According to our calculations, the low-frequency peak at 111 cm^{-1} is comprised of two modes with an additional lower-frequency mode at 83 cm^{-1}. Frequency versus pressure plots for these three modes, $E_2(1)$, $E_2(2)$, and $E_1(1)$, are shown in Fig. 4(b). Given the approximations in our calculations, the theoretical and experimental phonon frequencies can differ from each other. For purposes of comparison, we apply a rigid shift to the predicted phonon frequencies for each of the modes to match our experimental observation; qualita-

tively, the predicted behavior matches well with the observed trends.

Figure 5 displays the displacement patterns of the three modes that soften under pressure, obtained from calculations for $LuFeO_3$ and $ScFeO_3$ at zero pressure. All three modes are characterized by sliding motions of adjacent layers of the crystal structure against each other. The apical oxygens sitting above and below the iron oxide layer sit at crystallographically distinct sites, labeled as O1 and O2 in Fig. 5, respectively. Thus in the $E_2(1)$ mode [Fig. 5(a)], slabs of the crystal structure slide against each other with a shearing motion occurring between the iron-oxide layer and O2. In contrast, in the $E_2(2)$ mode [Fig. 5(b)] there is the same sliding of slabs, but the shearing is between the iron-oxide layer and
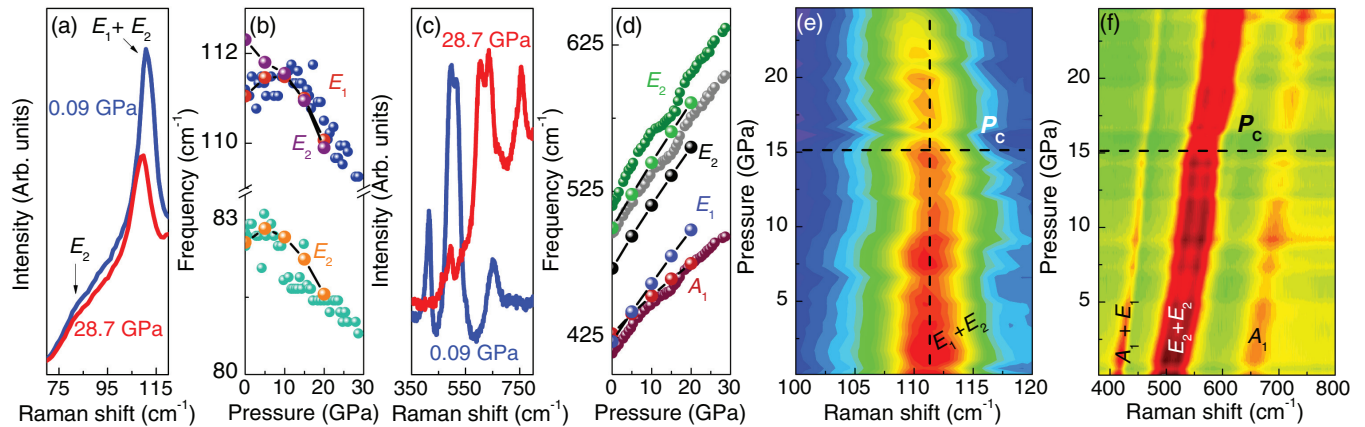

FIG. 4. (a) Close-up view of the low-frequency Raman response of $Lu_{0.6}Sc_{0.4}FeO_3$ in the low- and high-pressure phases. Mode assignments (E_2 and $E_1 + E_2$) are indicated. (b) Frequency vs pressure for the modes in (a) showing how they soften under pressure, consistent with our calculations. The theoretical data (red, purple, and orange spheres connected by black lines) have been rigidly shifted by a few wave numbers to overlap with the experimental results (blue and teal spheres). (c) Close-up view of the high-frequency Raman response of $Lu_{0.6}Sc_{0.4}FeO_3$ in the low- and high-pressure phases. (d) Frequency vs pressure results for the measurements in (c) along with complementary calculations. Theoretical modes are indicated by green, black, blue, and burgundy spheres connected with black lines with mode symmetries indicated in matching colors. Experimental points are given by green, gray, and maroon spheres. (e), (f) Contour plots summarize the pressure dependence of the low- and high-frequency Raman scattering response. Intensity is consistent across both plots and is represented by colors ranging from purple to red corresponding to low and high intensity, respectively. Mode assignments are indicated along the bottom, and the critical pressure is indicated by a horizontal dashed line. The vertical dashed line in (e) is a guide to the eye and highlights the mode softening.
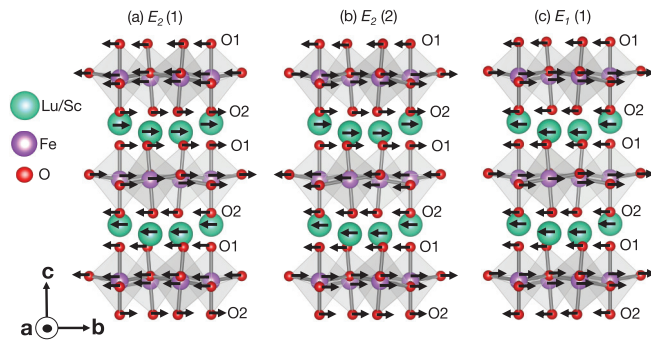
FIG. 5. Atomic displacements that contribute to the Raman active $E_2(1)$, $E_2(2)$, and $E_1(1)$ modes computed at zero pressure for the ground-state $P6_3cm$ structure of LuFeO$_3$ and ScFeO$_3$. The atomic displacement patterns of Lu$_{0.6}$Sc$_{0.4}$FeO$_3$ are qualitatively similar, as the primary effect of the mixed Lu/Sc composition is a change in mass.

O1. Finally, in the $E_1(1)$ mode [Fig. 5(c)], the iron-oxide and Lu/Sc layers slide against each other, where all Fe atoms and equatorial oxygens displace to the right, and all Lu atoms and apical oxygens displace to the left. The relative amplitudes of the Lu/Sc, Fe, apical oxygen, and equatorial oxygen displacements shown in Fig. 5 are different for LuFeO$_3$ and ScFeO$_3$, due to the mass difference between Lu and Sc (see the Supplemental Material for details [46]).

The presence of low-frequency Raman-active vibrational modes that soften under pressure suggests the possibility of negative thermal expansion. We therefore calculated mode Grüneisen parameters (γ_i) in order to quantify how the frequency shifts affect the unit-cell volume as

$$\gamma_i = \frac{B}{\omega_i} \frac{\partial \omega_i}{\partial P}. \qquad (5)$$

Here, B is the bulk modulus, ω_i is the frequency of a given mode, and $\partial \omega_i / \partial P$ is obtained by extracting the slope from frequency versus pressure plots in the high-pressure regime above P_C [55,56]. We employ the bulk modulus of LuFeO$_3$ in this calculation (220 GPa) [2]. Table S6 summarizes the γ_i's for both Raman- and infrared-active vibrational modes [46]. The main term of interest is γ_{av}, which is the mean of the individual mode Grüneisen parameters. This term (along with the molar heat capacity at constant volume and the bulk modulus) goes into the calculation of the coefficient of thermal expansion, α. Looking at the individual γ_i's, we note that the average takes a positive value, guaranteeing that α will also take a positive value. This rules out the existence of negative thermal expansion in Lu$_{0.6}$Sc$_{0.4}$FeO$_3$.

C. Structure-property relationships and comparison with the rare-earth manganites and other materials

To place our findings in context with other hexagonal oxides, we next compare our results with trends in related materials. Previous studies on other isostructural systems have generally reported a transition to the orthorhombic *Pbnm* phase under pressure. For example, work on *h*-YMnO$_3$ has shown that it stays in space group $P6_3cm$ up to 20 GPa and then converts to an orthorhombic *Pbnm* structure

[28,29]. Work on ErMnO$_3$ [30] and TmMnO$_3$ [31] reveals a hexagonal-orthorhombic crossover at somewhat lower pressures (17 and 10 GPa, respectively). Finally, high-pressure work on *h*-YInO$_3$ found a coexistence of the orthorhombic and hexagonal phases between 15 and 30 GPa [32].

In contrast with the hexagonal manganites and indites, we do not observe a transition to an orthorhombic space group in Lu$_{0.6}$Sc$_{0.4}$FeO$_3$. To rationalize this finding, we focus on a recent high-pressure x-ray emission study of hexagonal ferrites in which the pressure dependence of orthorhombic LuFeO$_3$ is compared with *h*-Lu$_{0.5}$Sc$_{0.5}$FeO$_3$ [3]. The measurements uncover that the orthorhombic system undergoes a pressure-driven spin-crossover from a high to low ($S = 5/2 \rightarrow S = 1/2$) spin state at 50 GPa [3]. Conversely, the same type of transition is completely absent for *h*-Lu$_{0.5}$Sc$_{0.5}$FeO$_3$, demonstrating that the Fe remains in a trigonal bipyramidal environment up to at least 60 GPa (and very likely more according to theory) [3]. This study suggests that our search for symmetry in the high-pressure phase in Lu$_{0.6}$Sc$_{0.4}$FeO$_3$ should exclude orthorhombic space groups. Work on compressively strained *h*-LuFeO$_3$ films allows us to further bolster our selection of the high-pressure space group. Beyond revealing how pressure increases the K_3 order-parameter amplitude, this study describes how the polarization of the hexagonal films is proportional to the amplitude of the K_3 order parameter [23]. Given that the $P6_3/mmc$ space group is centrosymmetric and that the K_3 mode is highly unstable within this structure, we can exclude it as a possible symmetry for the high-pressure phase. Taken together, these studies strengthen our claim of a $P6_3cm \leftrightarrow P\bar{3}c1$ pressure-induced structural phase transition at 15 GPa in Lu$_{0.6}$Sc$_{0.4}$FeO$_3$.

To further explore mechanisms that stabilize the high-pressure phase of Lu$_{0.6}$Sc$_{0.4}$FeO$_3$, we make use of our first-principles calculations to compute the enthalpy difference between various structural phases as a function of pressure for the LuFeO$_3$ and ScFeO$_3$ end-member compounds (see the Supplemental Material [46]). We find that for both materials, increasing pressure strongly stabilizes *Pbnm*, that is, the enthalpy difference between *Pbnm* and $P6_3cm$ becomes more negative with increasing pressure. In contrast, the enthalpy difference between $P\bar{3}c1$ and $P6_3cm$ is positive and becomes slightly more positive as pressure increases. This result clearly contrasts with our analysis of Fig. 3, where we find that $P\bar{3}c1$ shows the superior match between experimental and theoretical spectra in the high-pressure phase. We hypothesize that mixed Lu/Sc cations on the *A*-site in Lu$_{0.6}$Sc$_{0.4}$FeO$_3$ may play a key role in stabilizing the hexagonal structure up to high pressures. Our reasons for this conjecture are as follows. First, we note that the hexagonal structure is a metastable phase for the ferrites, and the mixed Lu/Sc cations on the *A*-site are known to enable synthesis of the hexagonal phase at ambient conditions [18]. We expect that this stabilizing influence of the mixed Lu/Sc on the hexagonal structure would persist under pressure.

Second, we note that the orthorhombic *Pbnm* structure, which has been reported as the high-pressure phase for manganites and indites with single *A*-site cations, has one crystallographically distinct *A*-site. In contrast, the hexagonal $P6_3cm$ and $P\bar{3}c1$ structures have two crystallographically

distinct A-sites. Due to this idiosyncrasy, we expect that the hexagonal structures may more easily accommodate a mixture of A-site cations of different sizes. Analysis of A-O polyhedra in our DFT-relaxed LuFeO$_3$ structures reveals that the two distinct A-sites in $P6_3cm$ are fairly similar (in terms of polyhedral volume and bond lengths), whereas there is a bigger difference between the two A-sites in $P\bar{3}c1$. In particular, there is a distinction between the sites where the A-cation displaces up/down toward the adjacent iron-oxide layer, and the sites where the A cation does not displace (see Fig. 1). The result is that in the first A-site there is a short (2.32 Å) bond between the A-cation and the planar oxygen it displaces towards, and a long (3.48 Å) bond between the A-cation and the layer it moves away from. In the second type of A-site, the bonds with the planar oxygens in the upper/lower layers are the same (2.90 Å). These different bonding environments may allow $P\bar{3}c1$ to more readily accommodate a mixture of A-site cations of different sizes. Based on this discussion, we speculate that if the end-member hexagonal compounds LuFeO$_3$ and ScFeO$_3$ could be synthesized, then they would display a distinct pressure response compared to Lu$_{0.6}$Sc$_{0.4}$FeO$_3$: they would transition to $Pbnm$ in analogy with the manganites and indites.

Finally, comparison to temperature-dependent structural transitions in other hexagonal materials can provide additional insight, since temperature and pressure may access similar phases. Combined neutron scattering and theory work on YMnO$_3$ has shown that with increasing temperature it transitions from $P6_3cm$ to a phase where the phase Φ of the K_3 order parameter can take on any value, and this value varies locally within the structure [20]. As another example, electron microscopy work on InMnO$_3$ has shown that it transitions from $P6_3cm$ to $P\bar{3}c1$ upon heating (which arises from a change in Φ by $\pi/6$), with a mesoscale coexistence of these two phases in an intermediate temperature regime [57]. Thus the impact of temperature appears to modulate Φ, which controls the axis about which the bipyramids tilt, which suggests that this may also be tunable by other external parameters such as pressure.

IV. SUMMARY AND OUTLOOK

Hexagonal rare-earth ferrites are attracting significant attention due to their unique properties, which manifest from competing structural trends, as well as their use and future potential as building blocks for more complex systems. To explore these issues in a linear magnetoelectric, we combined diamond anvil cell techniques, synchrotron-based infrared absorption and Raman scattering spectroscopies, group theory, and lattice dynamics calculations to uncover a pressure-driven polar $\leftrightarrow$ antipolar transition in h-Lu$_{0.6}$Sc$_{0.4}$FeO$_3$. By comparing the measured and calculated vibrational properties, we unravel the symmetry change across the 15 GPa transition as $P6_3cm \leftrightarrow P\bar{3}c1$. At the same time, we analyze our findings in terms of the symmetry progression in related materials, and we show that the ferrites under pressure are significantly different from the manganites. This suggests opportunities to drive toward very different states of matter under other external stimuli as well.

[1] H. Das, A. L. Wysocki, Y. Geng, W. Wu, and C. J. Fennie, Bulk magnetoelectricity in the hexagonal manganites and ferrites, Nat. Commun. **5**, 2998 (2014).

[2] A. G. Gavriliuk, G. N. Stepanov, U. S. Lyubutin, A. S. Stepin, I. A. Trojan, and V. A. Sidorov, High pressure studies of magnetic, electronic, and local structure properties in the rare-earth orthoferrites RFeO$_3$ (R = Nd, Lu), Hyperfine Interact. **126**, 305 (2000).

[3] T. Wen, Y. Wang, C. Li, D. Jiang, Z. Jiang, S. Qu, W. Yang, and Y. Wang, Site-specific pressure-driven spin-crossover in Lu$_{1-x}$Sc$_x$FeO$_3$, J. Phys. Chem. Lett. **11**, 8549 (2020).

[4] M. Angst, R. P. Hermann, A. D. Christianson, M. D. Lumsden, C. Lee, M.-H. Whangbo, J.-W. Kim, P. J. Ryan, S. E. Nagler, W. Tian, R. Jin, B. C. Sales, and D. Mandrus, Charge Order in LuFe$_2$O$_4$: Antiferroelectric Ground State and Coupling to Magnetism, Phys. Rev. Lett. **101**, 227601 (2008).

[5] X. S. Xu, M. Angst, T. V. Brinzari, R. P. Hermann, J. L. Musfeldt, A. D. Christianson, D. Mandrus, B. C. Sales, S. McGill, J.-W. Kim, and Z. Islam, Charge Order, Dynamics, and Magnetostructural Transition in Multiferroic LuFe$_2$O$_4$, Phys. Rev. Lett. **101**, 227602 (2008).

[6] X. Shen, C. H. Xu, C. H. Li, Y. Zhang, Q. Zhao, H. Z. Yang, Y. Sun, J. Q. Li, C. Q. Jin, and R. C. Yu, Pressure effects on multiferroic LuFe$_2$O$_4$, Appl. Phys. Lett. **96**, 102909 (2010).

[7] C. M. Brooks, R. Misra, J. A. Mundy, L. A. Zhang, B. S. Holinsworth, K. R. O'Neal, T. Heeg, W. Zander, J. Schubert, J. L. Musfeldt, Z.-K. Liu, D. A. Muller, P. Schiffer, and D. G. Schlom, The adsorption-controlled growth of LuFe$_2$O$_4$ by molecular-beam epitaxy, Appl. Phys. Lett. **101**, 132907 (2012).

[8] W. Wu, V. Kiryukhin, H.-J. Noh, K.-T. Ko, J.-H. Park, W. Ratcliff II, P. A. Sharma, N. Harrison, Y. J. Choi, Y. Horibe, S. Lee, S. Park, H. T. Yi, C. L. Zhang, and S.-W. Cheong,

Formation of Pancake-Like Ising Domains and Giant Magnetic Coercivity in Ferrimagnetic LuFe$_2$O$_4$, Phys. Rev. Lett. **101**, 137203 (2008).

[9] M. H. Phan, N. A. Frey, M. Angst, J. de Groot, B. C. Sales, D. G. Mandrus, and H. Srikanth, Complex magnetic phases in LuFe$_2$O$_4$, Solid State Commun. **150**, 341 (2010).

[10] X. S. Xu, J. de Groot, Q.-C. Sun, B. C. Sales, D. Mandrus, M. Angst, A. P. Litvinchuk, and J. L. Musfeldt, Lattice dynamical probe of charge order and antipolar bilayer stacking in LuFe$_2$O$_4$, Phys. Rev. B **82**, 014304 (2010).

[11] J. A. Moyer, R. Misra, J. A. Mundy, C. M. Brooks, J. T. Heron, D. A. Muller, D. G. Schlom, and P. Schiffer, Intrinsic magnetic properties of hexagonal LuFeO$_3$ and the effects of nonstoichiometry, APL Mater. **2**, 012106 (2014).

[12] J. A. Mundy, C. M. Brooks, M. E. Holtz, J. A. Moyer, H. Das, A. F. Rebola, J. T. Heron, J. D. Clarkson, S. M. Disseler, Z. Liu, A. Farhan, R. Held, R. Hovden, E. Padgett, Q. Mao, H. Paik, R. Misra, L. F. Kourkoutis, E. Arenholz, A. Scholl *et al.*, Atomic engineering of ferroic layers to create a room-temperature magnetoelectric multiferroic, Nature (London) **537**, 523 (2016).

[13] R. Ramesh and D. G. Schlom, Creating emergent phenomena in oxide superlattices, Nat. Rev. Mater. **4**, 257 (2019).

[14] S. Fan, H. Das, A. F. Rebola, K. A. Smith, J. A. Mundy, C. S Brooks, M. Holtz, D. A. Muller, C. J. Fennie, R. Ramesh, D. G. Schlom, S. A. McGill, and J. L. Musfeldt, Site-specific spectroscopic measurement of spin and charge in (LuFeO$_3$)$_m$/(LuFe$_2$O$_4$)$_1$ multiferroic superlattices, Nat. Commun. **11**, 5582 (2020).

[15] M. E. Holtz, E. S. Padgett, R. Steinhardt, C. M. Brooks, D. Meier, D. G. Schlom, D. A. Muller, and J. A. Mundy, Dimensionality-Induced Change in Topological Order in Multiferroic Oxide Superlattices, Phys. Rev. Lett. **126**, 157601 (2021).

[16] K. Xu, X.-Z. Lu, and H.-J. Xiang, Designing new ferroelectrics with a general strategy, npj Quantum Mater. **2**, 1 (2017).

[17] T. Kurumaji, S. Ishiwata, and Y. Tokura, Doping-Tunable Ferrimagnetic Phase with Large Linear Magnetoelectric Effect in a Polar Magnet Fe$_2$Mo$_3$O$_8$, Phys. Rev. X **5**, 031034 (2015).

[18] K. Du, B. Gao, Y. Wang, X. Xu, J. Kim, R. Hu, F.-T. Huang, and S.-W. Cheong, Vortex ferroelectric domains, large-loop weak ferromagnetic domains, and their decoupling in hexagonal (Lu, Sc)FeO$_3$, npj Quantum Mater. **3**, 33 (2018).

[19] S. M. Disseler, J. A. Borchers, C. M. Brooks, J. A. Mundy, J. A. Moyer, D. A. Hillsberry, E. L. Thies, D. A. Tenne, J. Heron, M. E. Holtz, J. D. Clarkson, G. M. Stiehl, P. Schiffer, D. A. Muller, D. G. Schlom, and W. D. Ratcliff, Magnetic Structure and Ordering of Multiferroic Hexagonal LuFeO$_3$, Phys. Rev. Lett. **114**, 217602 (2015).

[20] S. H. Skjærvø, Q. N. Meier, M. Feygenson, N. A. Spaldin, S. J. L. Billinge, E. S. Bozin, and S. M. Selbach, Unconventional Continuous Structural Disorder at the Order-Disorder Phase Transition in the Hexagonal Manganites, Phys. Rev. X **9**, 031001 (2019).

[21] J. H. Lee, L. Fang, E. Vlahos, X. Ke, Y. W. Jung, L. F. Kourkoutis, J.-W. Kim, P. J. Ryan, T. Heeg, M. Roeckerath, V. Goian, M. Bernhagen, R. Uecker, P. C. Hammel, K. M. Rabe, S. Kamba, J. Schubert, J. W. Freeland, D. A. Muller, C. J. Fennie *et al.*, A strong ferroelectric ferromagnet created by means of spin-lattice coupling, Nature (London) **466**, 954 (2010).

[22] J. H. Lee and K. M. Rabe, Epitaxial-Strain-Induced Multiferroicity in SrMnO$_3$ from First Principles, Phys. Rev. Lett. **104**, 207204 (2010).

[23] K. Sinha, Y. Zhang, X. Jiang, H. Wang, X. Wang, X. Zhang, P. J. Ryan, J.-W. Kim, J. Bowlan, D. A. Yarotski, Y. Lu, A. D. DiChiara, X. Cheng, X. Wu, and X. Xu, Effects of biaxial strain on the improper multiferroicity in *h*-LuFeO$_3$ films studied using restrained thermal expansion method, Phys. Rev. B **95**, 094110 (2017).

[24] K. Sinha, H. Wang, X. Wang, L. Zhou, Y. Yin, W. Wang, X. Cheng, D. J. Keavney, H. Cao, Y. Liu, X. We, and X. Xu, Tuning the Néel Temperature of Hexagonal Ferrites by Structural Distortion, Phys. Rev. Lett. **121**, 237203 (2018).

[25] C. J. Fennie and K. M. Rabe, Ferroelectric transition in YMnO$_3$ from first principles, Phys. Rev. B **72**, 100103(R) (2005).

[26] W. Wang, J. Zhao, W. Wang, Z. Gai, N. Balke, M. Chi, H. N. Lee, W. Tian, L. Zhu, X. Cheng, Da. J. Keavney, J. Yi, T. Z. Ward, P. C. Snijders, H. M. Christen, W. Wu, J. Shen, and X. Xu, Room-Temperature Multiferroic Hexagonal LuFeO$_3$ films, Phys. Rev. Lett. **110**, 237601 (2013).

[27] F.-T. Huang, X. Wang, S. M. Riffin, Y. Kamagai, O. Gindele, M.-W. Chu, Y. Horibe, N. Spaldin, and S.-W. Cheong, Duality of Topological Defects in Hexagonal Manganites, Phys. Rev. Lett. **113**, 267602 (2014).

[28] S. H. Jabarov, N. T. Dang, S. E. Kichanov, D. P. Kozlenko, L. S. Dubrovinsky, J.-G. Park, S. Lee, A. I. Mammadov, R. Z. Mehdiyeva, B. N. Savenko, N. X. Nghia, L. H. Khiem, N. T. T. T. Lieu, and L. T. P Thao, Crystal structure and vibrational spectra of hexagonal manganites YMnO$_3$ and LuMnO$_3$ under high pressure, Mater. Res. Express **6**, 086110 (2019).

[29] P. Gao, Z. Chen, T. A. Tyson, T. Wu, K. H. Ahn, Z. Liu, R. Tappero, S. B. Kim, and S.-W. Cheong, High-pressure structural stability of multiferroic hexagonal RMnO$_3$ (R = Y, Ho, Lu), Phys. Rev. B **83**, 224113 (2011).

[30] C. Lin, J. Liu, X. Li, Y. Li, S. Chu, L. Xiong, and R. Li, Phase transformation in hexagonal ErMnO$_3$ under high pressure, J. Appl. Phys. **112**, 113512 (2012).

[31] L. J. Wang, S. M. Feng, J. L. Zhu, Q. Q. Liu, Y. C. Li, X. D. Li, J. Liu, and C. Q. Jin, Structure transition of multiferroic hexagonal TmMnO$_3$ compound under high pressure, High Press. Res. **30**, 258 (2010).

[32] A. Dwivedi, H. K. Poswal, R. Shukla, S. Velaga, B. D. Sahoo, V. Grover, and M. N. Deo, High pressure structural investigations on hexagonal YInO$_3$, High Press. Res. **39**, 17 (2019).

[33] J. Ruiz-Fuertes, B. Winkler, T. Bernert, L. Bayarjargal, W. Morgenroth, M. Koch-Müller, K. Refson, V. Milman, and N. Tamura, Ferroelectric soft mode of polar ZnTiO$_4$ investigated by Raman spectroscopy at high pressure, Phys. Rev. B **91**, 214110 (2015).

[34] H.-H. Kung, R. E. Baumbach, E. D. Bauer, V. K. Thorsmolle, W.-L. Zhang, K. Haule, J. A. Mydosh, and G. Blumberg, Chirality density wave of the "hidden order" phase in URu$_2$Si$_2$, Science **347**, 1339 (2015).

[35] D. V. S. Muthu, P. Teredesai, S. Saha, W. U. V. Suchitra, A. K. Sood, and C. N. R. Rao, Pressure-induced structural phase transitions and phonon anomalies in ReO$_3$: Raman and first-principles study, Phys. Rev. B **91**, 224308 (2015).

[36] K. Kim, S. Y. Lim, J.-U. Lee, S. Lee, T. Y. Kim, K. Park, G. S. Jeon, C.-H. Park, J.-G. Park, and H. Cheong, Suppression of

magnetic ordering in XXZ-type antiferromagnetic monolayer NiPS$_3$, Nat. Commun. **10**, 345 (2019).

[37] H. K. Mao, J. Xu, and P. M. Bell, Calibration of the ruby pressure gauge to 800 kbar under quasi-hydrostatic conditions, J. Geophys. Res. **91**, 4673 (1986).

[38] S. Venugopalon and M. M. Becker, Raman scattering study of LuFeO$_3$, J. Chem. Phys. **93**, 3833 (1990).

[39] P. Hohenberg and W. Kohn, Inhomogeneous electron gas, Phys. Rev. **136**, B864 (1964).

[40] V. I. Anisimov, F. Aryasetiawan, and A. I. Lichtenstein, First-principles calculations of the electronic structure and spectra of strongly correlated systems: the LDA+ U method, J. Phys.: Condens. Matter **9**, 767 (1997).

[41] P. E. Blochl, Projector augmented-wave method, Phys. Rev. B **50**, 17953 (1994).

[42] G. Kresse and J. Furthmüller, Efficient iterative schemes for ab initio total-energy calculations using a plane-wave basis set, Comp. Mater. Sci. **6**, 15 (1996).

[43] A. I. Lichtenstein, V. I. Anisimov, and J. Zaanen, Density-functional theory and strong interactions: Orbital ordering in Mott-Hubbard insulators, Phys. Rev. B **52**, R5467 (1995).

[44] H. Das, A. L. Wysocki, Y. Geng, W. Wu, and C. J. Fennie, Direct visualization of magnetoelectric domains, Nat. Mater. **13**, 163 (2014).

[45] J. P. Perdew, A. Ruzsinszky, G. I. Csonka, O. A. Vydrov, G. E. Scuseria, L. A. Constantin, X. Zhou, and K. Burke, Restoring the Density-Gradient Expansion for Exchange in Solids and Surfaces, Phys. Rev. Lett. **100**, 136406 (2008).

[46] See Supplemental Material at http://link.aps.org/supplemental/10.1103/PhysRevB.104.094109 for additional details about the calculations, justification for the assignment of the high-pressure phase, and Grüneisen parameter analysis.

[47] P. Giannozzi, S. de Gironcoli, Stefano, P. Pavone, and S. Baroni, Ab initio calculation of phonon dispersions in semiconductors, Phys. Rev. B **43**, 7231 (1991).

[48] X. Gonze, First-principles responses of solids to atomic displacements and homogeneous electric fields: Implementation of a conjugate-gradient algorithm, Phys. Rev. B **55**, 10355 (1997).

[49] X. Gonze and C. Lee, Dynamical matrices, Born effective charges, dielectric permittivity tensors, and interatomic force constants from density-functional perturbation theory, Phys. Rev. B **55**, 10337 (1997).

[50] A. Togo, F. Oba, and I. Tanaka, First-principles calculations of the ferroelastic transition between rutile-type and CaCl$_2$-type SiO$_2$ at high pressures, Phys. Rev. B **78**, 134106 (2008).

[51] A. Togo, L. Chaput, and I. Tanaka, Distributions of phonon lifetimes in Brillouin zones, Phys. Rev. B **91**, 094306 (2015).

[52] J. M. Skelton, L. A. Burton, A. J. Jackson, F. Oba, S. C. Parker, and A. Walsh, Lattice dynamics of the tin sulphides SnS$_2$, SnS and Sn$_2$S$_3$: Vibrational spectra and thermal transport, Phys. Chem. Chem. Phys. **19**, 12452 (2017).

[53] J. M. Skelton, https://github.com/JMSkelton/Phonopy-Spectroscopy.

[54] D. Porezag and M. R. Pederson, Infrared intensities and Raman-scattering activities within density-functional theory, Phys. Rev. B **54**, 7830 (1996).

[55] E. T. Ritz and N. A. Benedek, Interplay Between Phonons and Anisotropic Elasticity Drives Negative Thermal Expansion in PbTiO$_3$, Phys. Rev. Lett. **121**, 255901 (2018).

[56] N. W. Ashcroft and N. D. Merman, in *Solid State Physics*, edited by D. G. Crane (Saunders College, Philadelphia, 1976), p. 493.

[57] F.-T. Huang, X. Wang, Y. S. Oh, K. Kurushima, S. Mori, Y. Horibe, and S.-W. Cheong, Delicate balance between ferroelectricity and antiferroelectricity in hexagonal InMnO$_3$, Phys. Rev. B **87**, 184109 (2013).